Supplement of The Cryosphere, 18, 3741–3763, 2024
https://doi.org/10.5194/tc-18-3741-2024-supplement

The Cryosphere Open Access EGU

Supplement of

On the relationship between $\delta O_2/N_2$ variability and ice sheet surface conditions in Antarctica

Romilly Harris Stuart et al.

Correspondence to: Romilly Harris Stuart (romilly.harris-stuart@lsce.ipsl.fr)

S1 $\delta O_2/N_2$ datasets and gas loss effects

S1.1 Data validation

Table S1 and Table S2 present information about the published and unpublished $\delta O_2/N_2$ datasets, respectively. Each of the datasets are plotted versus depth in Fig. S1, with grey markers indicating the entire datasets and coloured points indicating the data remaining after applying the data rejection criteria in Section 2.2.3 of the main text. Given the incomplete storage history of each ice core, we do not attempt to correct for gas loss effects in clathrate ice. Instead, measurements on clathrate ice stored above -50°C for more than three years are rejected from our analysis (see Section S1.2). However, Bender (2002) observed characteristics of gas loss effected $\delta O_2/N_2$ values in bubble ice from Vostok which they attribute to selective loss of O_2 via microcracks in the ice following coring. This led to the removal of the bubble ice $\delta O_2/N_2$ data from Vostok (Fig. S1). Measurements on clathrate ice presented in Suwa and Bender (2008a) were corrected for gas loss effects using the earlier data from Bender (2002), and thus were included in our study.

Measurements of $\delta O_2/N_2$ in samples from the bubble clathrate transition zones (BCTZ) must also be identified and removed from to avoid associated biases (Section 2.2.3 in main text). We take a conservative approach and remove all data falling within the BCTZ as it is the absolute values which we are comparing between sites. Differentiating the BCTZ from the brittle ice zones (such as those reported in Neff (2014)) is not trivial and makes the rejection of data from such zones somewhat subjective. To minimise this risk, we first identify sites without clathrate hydrates–and thus, by definition, without BCTZs–but which reportedly have brittle zones. These sites are as follows: BI (Mulvaney et al., 2007), DE08 (Etheridge et al., 1996), and RICE (Lee et al., 2020). Data from DE08 comes from samples above the reported brittle zone and are therefore included. While the data from BI fall within the brittle zone, there is little evidence for fractionation associated with bubble-clathrate transition and so these data are included. The BCTZ in the RICE core reportedly starts from 763 m (Lee et al., 2020), which corresponds to the bottom of the core. Some of the deepest samples appear increasingly depleted in $\delta O_2/N_2$ compared to shallower samples. Given that the $\delta O_2/N_2$ measurements were performed more than 4 years after the core was drilled, and that the ice was stored above -50°C, we expect that these samples were influenced by gas loss and therefore remove them from our analysis (Fig. S2). The influence of gas loss is further explored in the following section.

Table S1. Information on published datasets used in this study. Core storage history are presented to the best of our knowledge.

Site	Cored (yr)	Measured (yr)	Storage temp. (°C)	Depth (m)	Zone	Reference
Dome Fuji	1993–1996	2006	-50	1204.05–2500.36	All	Kawamura et al. (2007)
Dome Fuji	1993–1996	2017	-50	112.99–2001.06	All	Oyabu et al. (2021a)
EPICA Dome C	1999–2004	2005–2008	-50		Clathrate	Landais et al. (2012)
EPICA Dome C	1999–2004	2016	-50	1400.82–3188.87	Clathrate	Extier et al. (2018)
EPICA Dome C	1999–2004	2021–2022	-50		Clathrate	Bouchet et al. (2023)
GISP2	1989–1993	1993	-35	72.85–2235.05	All	Bender et al. (1994)
GISP2	1989–1993	1994	-35	117.7–3032	All	Smith, 1998
GISP2	1989–1993	2006	-35	274.24–2287.88	All	Suwa and Bender (2008b)
Law Dome DE08	1987	2017-2020	-	175.15–218.2	Bubble	Buizert et al. (2020)
Law Dome DSSW20k	1997	2017-2020	-	60.88–63.08	Bubble	Buizert et al. (2020)
NGRIP	1996–2004	2012	-20	2464.09–2591.69	Clathrate	Bazin et al. (2016)
Roosevelt Island	2011–2013	2017-2020	-36	116–146	Bubble	Buizert et al. (2020)
Roosevelt Island	2011–2013	2017	-36	60.2–761	Bubble	Lee et al. (2020)
Siple Dome (SDM94)	1994–2995	2017-2020	-25	69.22–69.66	Bubble	Buizert et al. (2020)
Siple Dome (SDMA)	1997–1999	∼2008	-25	74.95–972.98	All	Severinghaus (2009)
South Pole	2014–2016	2017-2020	-35	158–188.35	Bubble	Buizert et al. (2020)
South Pole	2014–2016	2019	-35	125.3–1751.01	All	Severinghaus (2019)
TALDICE	2005–2007	2020	-20	1356–1617	All	Crotti et al. (2021)
Vostok	1990–1998	∼2001	-35	174.5–3348	All	Bender (2002)
Vostok	1990–1998	∼2006	-35	1595–3400	All	Suwa and Bender (2008a)
WAIS-Divide	2006–2011	2011	-35	80.29–3396.61	All	Severinghaus (2015)
WAIS-Divide	2006–2011	2017-2020	-35	119.35–190	Bubble	Buizert et al. (2020)

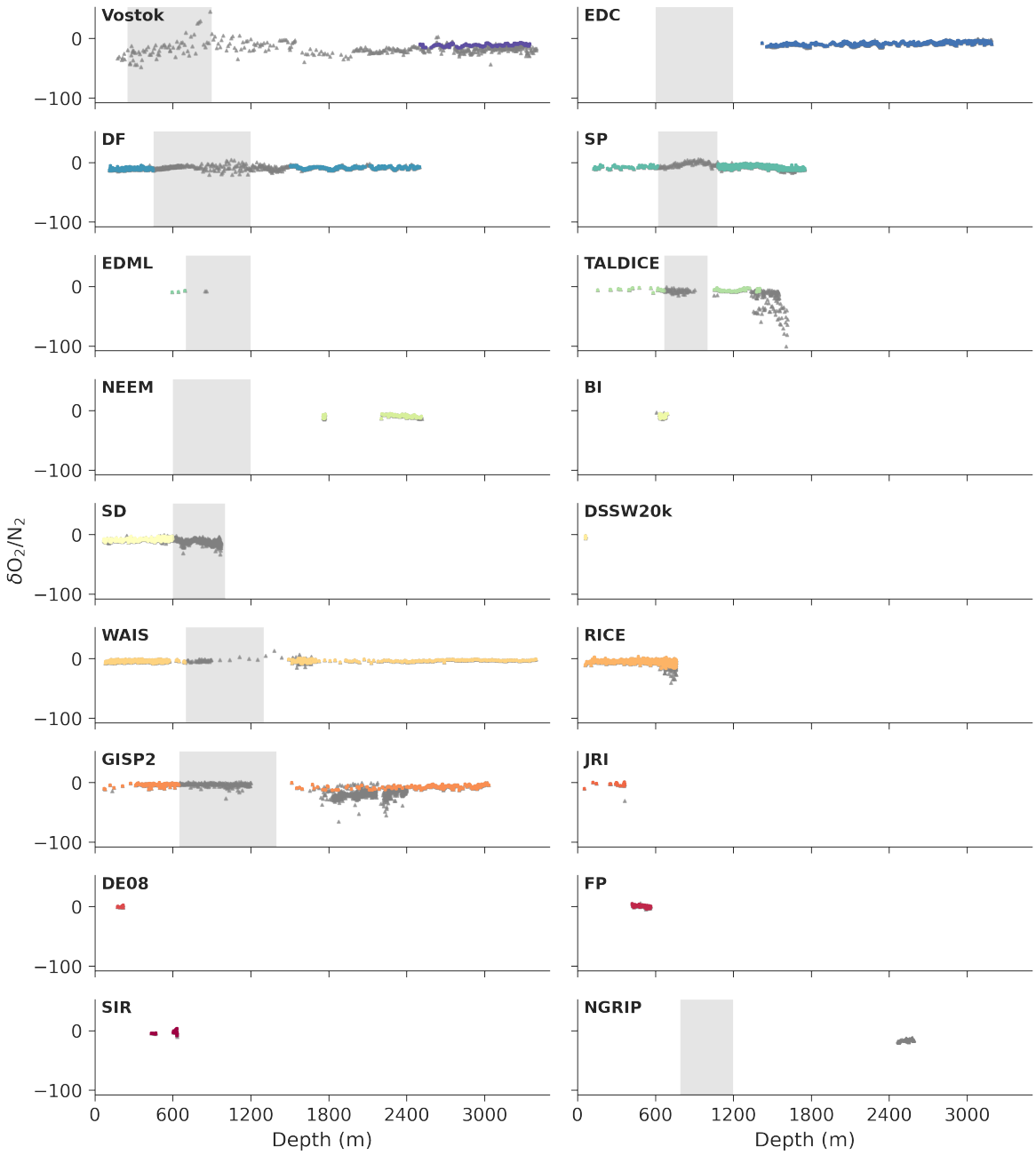

Figure S1. $\delta O_2/N_2$ records plotted against depth for all sites. Grey markers show all measurements before applying the correction criteria in Section 2.2.3 of the main text. Coloured markers indicate all data remaining after the removal of measurements from the BCTZ, those likely influenced by gas loss, and, subsequently, those falling 2σ from the mean for each respective site. Grey bars indicate reported bubble-clathrate transition zones for each site (Table 1 in main text).

Table S2. Information on unpublished datasets used in this study. Core history and measurement information are presented to the best of our knowledge. The laboratory at which the measurements were performed and the method used are also stated, where M-RF stands for melt refreeze method and ME for melt extraction method.

Site	Drilled (yr)	Measured (yr)	Storage temp. (°C)	Lab	Method	Depth range (m)	Zone
Berkner Island	2003–2005	2010–2011	-22	LSCE	M-RF	608.85–693.55	Bubble
EDML	2000–2006	2007	-25	LSCE	ME	596–860	Bubble
Fletcher Promontory	2011–2012	2015	-22	LSCE	ME	289.3–387.75	Bubble
GISP2	1989–1993	2009	-35	Scripps	M-RF	318.67–1201.22	All
GISP2	1989–1993	2017–2019	-35	Scripps	M-RF	1740.27–2399.45	Clathrate
James Ross Island	2008	2011	-22	LSCE	ME	52.25-363.55	Bubble
NEEM	2008–2012	2011	-20	LSCE	M-RF	1757.25–2524.5	Clathrate
Skytrain Ice Rise	2018–2019	2021	-22	LSCE	ME	299.75–436.15	Bubble
TALDICE	2005–2007	2008	-20	LSCE	ME	1003–1291	Clathrate
TALDICE	2005–2007	2009	-20	LSCE	M-RF	797.93–1401.92	BCTZ & clathrate
TALDICE	2005–2007	2010	-20	LSCE	M-RF	793.62–902.93	BCTZ
TALDICE	2005–2007	2011	-20	LSCE	ME	1472.92–1550.92	Clathrate
TALDICE	2005–2007	2012	-20	LSCE	ME	1527.95–1553.95	Clathrate
TALDICE	2005–2007	2019	-20	LSCE	ME	1551–1617	Clathrate
TALDICE	2005–2007	2022	-20	LSCE	ME	155–620	Bubble

S1.2 GISP2 and TALDICE $\delta O_2/N_2$ data

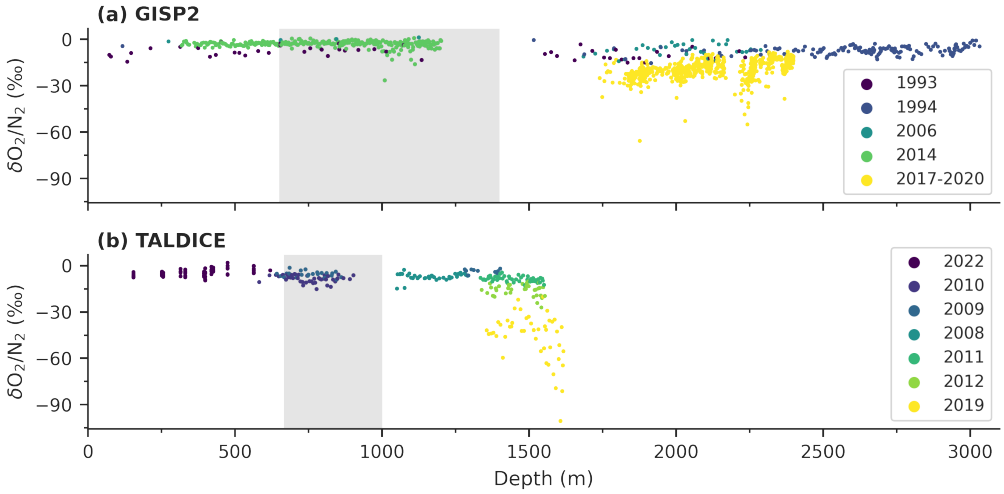

Figure S2. $\delta O_2/N_2$ series from a) the GISP2 ice core and b) the TALDICE ice core after different storage conditions. Colours represent the different measurement campaigns by year. Grey shaded regions represented the reported brittle zones (Neff, 2014).

Successive measurements on clathrate ice shows $\delta O_2/N_2$ depletion through time both from the GISP2 and TALDICE ice cores. A similar effect has been documented at EDC by Bouchet et al. (2023). There is also a depletion of up to 20‰ in measurements from between 2017 and 2020 (this study). Data from bubbly ice and within the reported brittle zone shows no gas loss effect. We note that measurements on the GISP2 core from Suwa and Bender (2008b) in 2006 were corrected using the measurements made more than 10 years earlier by Smith (1998).

For the TALDICE ice core, all measurements have been performed on the melt extraction line and storage was only possible at -20°C. Figure S2 shows the series of $\delta O_2/N_2$ measured after different periods of storage at -20°C. There is a clear depletion in $\delta O_2/N_2$ associated with storage time at -20°C, as explained in Ikeda-Fukazawa et al. (2004). Measurements performed on clathrate ice after 13 years (measured in 2019) show much more depletion than those measured 2 years after drilling (measured in 2008). However, we find that the mean value of $\delta O_2/N_2$ in the bubbly ice is consistent between measurement campaigns over 16 years of storage at -20°C. Therefore, we assume little or no gas loss for bubbly ice, at least in the TALDICE ice core.

S2 Temporal variability in $\delta O_2/N_2$ records from Dome Fuji and South Pole

We apply the same filtering method as described in Section 3.1.2 in the main text to the Dome Fuji and South Pole ice core data. For Dome Fuji, we only include data that corresponds to the most recent chronology which was synchronised to SSI (Oyabu et al., 2022). The South Pole ice core records use the SP19 chronology, which was constructed using layer counting and therefore is not tuned to SSI (Winski et al., 2019). As stated in the main text, measurements from the BCTZ are removed

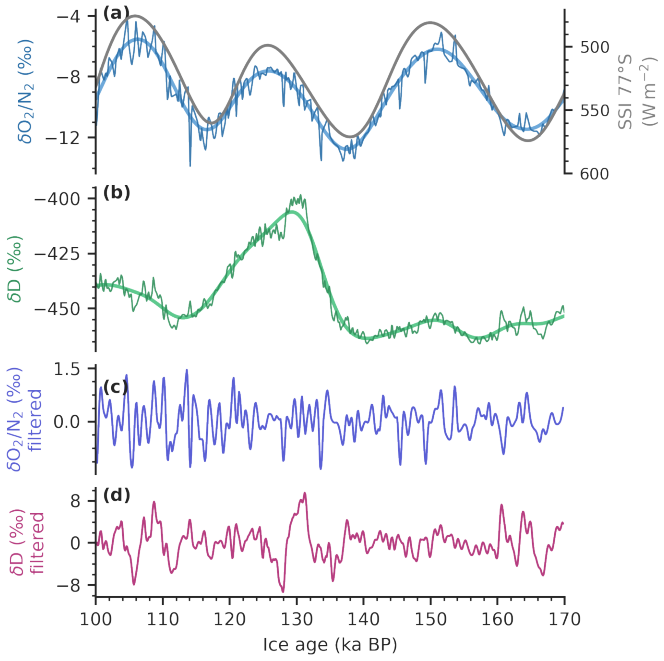

Figure S3. Time series of $\delta O_2/N_2$2, δD, and SSI on the DF-2021 ice-age chronology from Dome Fuji (Oyabu et al., 2022). Panel (a) presents the 100-year interpolated $\delta O_2/N_2$ overlain with the low pass filtered curve (blue). The right y-axis in panel (a) shown SSI at 77°S (grey). Panel (b) shows the 100-year interpolated δD overlain with the low pass filtered curve (green). The bottom two panels present the residuals of the low pass filtered curves for $\delta O_2/N_2$ (c) and δD (d).

leaving the data from 100–207 ka BP at Dome Fuji, and 18–54 ka BP at South Pole. Note that the DF-2021 chronology for Dome Fuji goes only until 207 ka BP. An average measurement resolution of ∼330 years on the Dome Fuji core between 100–170 ka BP is approximately the same as for EDC between 189–258 ka BP. The high accumulation rate at South Pole allows for a significantly higher resolution of ∼57 years.

Figure S3 presents data from the Dome Fuji core, with the high frequency signals of $\delta O_2/N_2$ and δD in the bottom two panels. Data older than 170 ka BP are of too low resolution for analysis of millennial-scale variability. Between 100 ka BP and 120 ka BP the filtered $\delta O_2/N_2$ records from Dome Fuji show a similar millennial-scale coherence to the filtered δD record. However, the rapid, high-frequency variability in $\delta O_2/N_2$ over this period may be attributed to scattering effects below the BCTZ, as was documented by Oyabu et al. (2021b). The rapid δD peak around 130 ka BP (corresponding to MIS 5) is not present in the $\delta O_2/N_2$ data. The absence of a 100 kyr climate signal in $\delta O_2/N_2$ records from Dome Fuji has been previously identified by Kawamura et al. (2007).

Figure S4 shows the data from South Pole. High-resolution measurements over the ∼34 kyr period from 18–52 ka BP reveal interesting signals which appear to be present in both the $\delta O_2/N_2$ and δD records. The $\delta O_2/N_2$ and δD filtered curves appear to resemble each other to varying degrees throughout the record, with the younger section (18–25 ka BP) varying quasi-in-

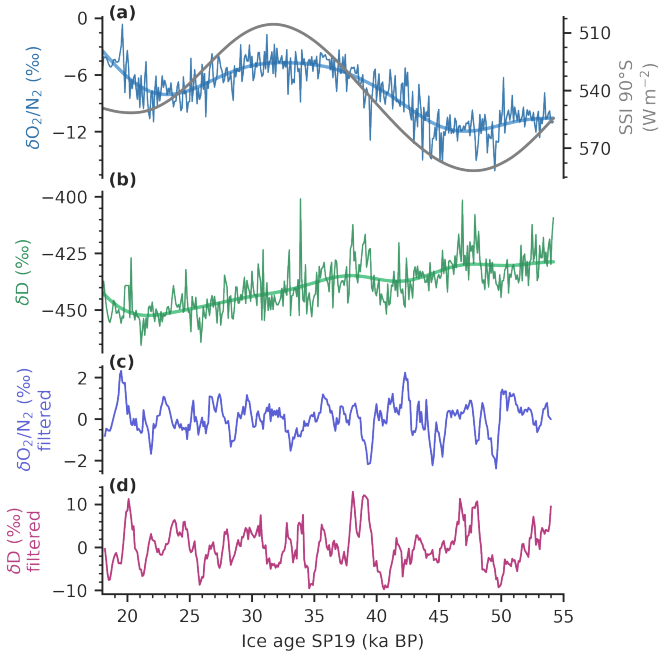

Figure S4. Time series of $\delta O_2/N_2$, δD, and SSI on the SP19 ice-age chronology from South Pole (Winski et al., 2019). Panel (a) presents the 100-year interpolated $\delta O_2/N_2$ overlain with the low pass filtered curve (blue). The right y-axis in panel (a) shown SSI at 90°S (grey). Panel (b) shows the 100-year interpolated δD overlain with the low pass filtered curve (green). The bottom two panels present the residuals of the low pass filtered curves for $\delta O_2/N_2$ (c) and δD (d).

phase, while the older section appears to be anti-phased, and often with δD lagging $\delta O_2/N_2$ (e.g., 46–52 ka BP). The in-phase coherence during the younger period also corresponds to relatively low δD, and hence, accumulation rate. Indeed, during the last glacial maximum at South Pole the accumulation rate was closer to that of EDC today ($\sim$3 cm yr^{-1} water equivalent; Kahle et al., 2020). δD is higher during the older period, potentially suggesting that a different mechanism is dominant under high accumulation conditions, as observed by Epifanio et al. (2023) for total air content.

S3 Crocus model temperature evaluation

Figure S5 shows the simulated snow temperature distributions over the top 20 cm for the different forcing scenarios. Summer snow temperatures are most sensitive to perturbations in shortwave radiation forcings (SSI), but there is negligible effect in winter due to polar night conditions remaining constant between forcings. Perturbations in accumulation rate appear to have little influence on snow temperature. In contrast, snow temperature is strongly modified by perturbations in air temperature, specifically during winter and in the decreased temperature scenario (T min). Interestingly, the increased temperature scenario (T max) does not substantially influence summer snow temperatures. Figure S5b, showing the daily mean snow temperatures

over the top 20 cm, further highlights the non-linear effects of temperature increase where T max results in negligible change in summer temperatures and higher winter temperatures than the reference simulation. As discussed in the main body of text, this is expected to be due to the increased sensitivity of snow temperatures to insolation.

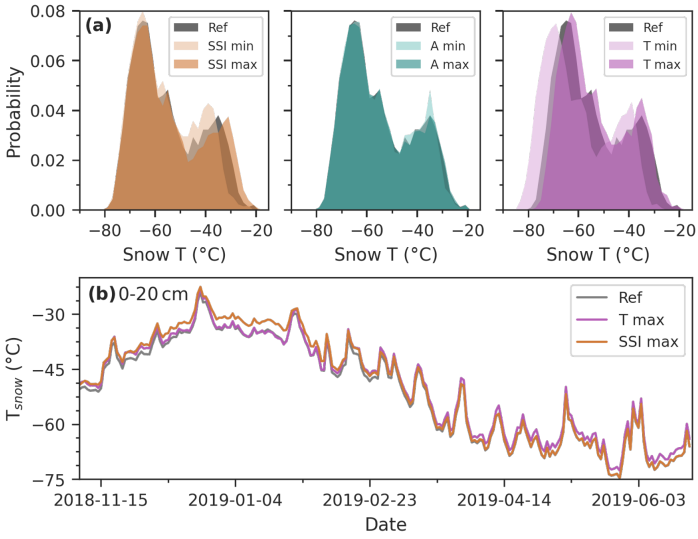

Figure S5. Comparison of simulated snow temperatures in the upper 20 cm at Dome C. Panel a) shows the distributions for each set of simulation; SSI (orange), accumulation rate (green) and temperature (purple) the reference simulation (grey); compared to the reference simulation (grey). A comparison of mean 20 cm snow temperature from the reference (grey), increased temperature (T max), and increase SSI (SSI max) simulations are shown in panel b) between November 2018 and June 2019.

S4 Interactions between surface forcings, physical properties, and close-off fractionation

Section 4.3 in the main text begins to draw links between the observed spatial and temporal variability in $\delta O_2/N_2$ records and surface surface snow properties. Figure S6 illustrates some of the observed and theoretical interactions outlined in that section. We note that this is an oversimplification of complex interactions, and is by no means exhaustive. Unnumbered lines are based on the results of this study. The numbers represent the following (often hypothesised) links:

[1] Permeability of firn is understood to largely control size dependent fractionation during pore closure, such that the more higher the permeability (and for extended time), the more depleted $\delta O_2/N_2$ in trapped bubbles (Ikeda-Fukazawa et al., 2004; Huber et al., 2006; Severinghaus and Battle, 2006).

[2] The permeability of firn can be described as a function of density and grain size (Gregory et al., 2014; Calonne et al., 2022). For a given density, layers with larger grain size are more permeable than those with small grain size. Moreover, the layer characteristics determine the depth of bubble close-off, with large grained layers closing off deeper

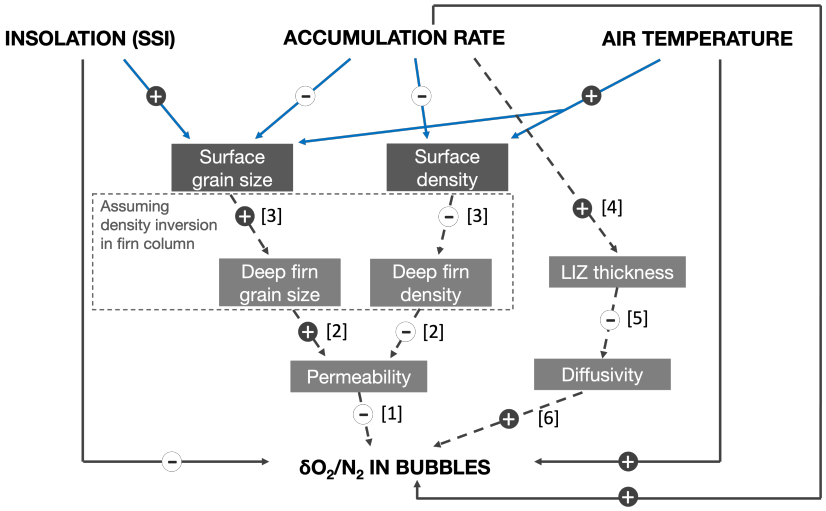

Figure S6. Schematic to show interactions between surface forcings, physical properties, and close-off fractionation. Plus signs show a direct relationship (i.e., increase in SSI corresponds to increase in grain size), and minus signs indicate an inverse relationship. Full lines indicate results from this study, with blue lines illustrating results from the Crocus model, and full black lines showing results from data analysis. Dashed lines show links based on previous studies, the numbers for which can be found in the text with associated references.

than fine grained (Gregory et al., 2014), and hence, allowing more time for gases to permeate out of large grained layers (Severinghaus and Battle, 2006; Fujita et al., 2009).

[3] Linking deep firn density and grain size to near-surface is not trivial, but in general, sites with large grains at the surface will be characterised by large grains in the deep firn (Gregory et al., 2014). In contrast, layers with relatively high near-surface density often correspond to layers with relatively low density (compared to the initially low density layers near the surface) in deep firn (Freitag et al., 2004). Such a density inversion is not present at all sites. For example, no density inversion was observed at Megadunes (Gregory et al., 2014), which likely relates to the zero-accumulation conditions.

[4] Lock-in zone (LIZ) thickness is increased with accumulation rate (Landais et al., 2006; Hörhold et al., 2011), which is attributed to enhanced density (and microstructural) layering in the deep firn (Landais et al., 2006; Fujita et al., 2009; Hörhold et al., 2011).

[5] Sites characterised by a thicker LIZ are expected to have higher pore space tortuosity (Fujita et al., 2009), or more complex pore space geometry (Gregory et al., 2014), which would presumably lead to reduced diffusivity.

[6] $\delta O_2/N_2$ depletion in bubbles requires that the O_2 enriched air in neighbouring open porosity can be efficiently re-mixed back into the open porous network. Therefore, reduced diffusivity within highly tortuous deep firn would impede the removal of O_2 enriched air, leading to the trapping of relatively enriched $\delta O_2/N_2$ in bubbles.

References

Bazin, L., Landais, A., Capron, E., Masson-Delmotte, V., Ritz, C., Picard, G., Jouzel, J., Dumont, M., Leuenberger, M., and Prié, F.: Phase relationships between orbital forcing and the composition of air trapped in Antarctic ice cores, Climate of the Past, 12, 729–748, https://doi.org/10.5194/cp-12-729-2016, 2016.

Bender, M. L.: Orbital tuning chronology for the Vostok climate record supported by trapped gas composition, Earth and Planetary Science Letters, 204, 275–289, https://doi.org/https://doi.org/10.1016/S0012-821X(02)00980-9, 2002.

Bender, M. L., Tans, P. P., Ellis, J., Orchardo, J., and Habfast, K.: A high precision isotope ratio mass spectrometry method for measuring the O2N2 ratio of air, Geochimica et Cosmochimica Acta, 58, 4751–4758, https://doi.org/https://doi.org/10.1016/0016-7037(94)90205-4, 1994.

Bouchet, M., Landais, A., Grisart, A., Parrenin, F., Prié, F., Jacob, R., Fourré, E., Capron, E., Raynaud, D., Lipenkov, V. Y., Loutre, M.-F., Extier, T., Svensson, A., Legrain, E., Martinerie, P., Leuenberger, M., Jiang, W., Ritterbusch, F., Lu, Z.-T., and Yang, G.-M.: The Antarctic Ice Core Chronology 2023 (AICC2023) chronological framework and associated timescale for the European Project for Ice Coring in Antarctica (EPICA) Dome C ice core, Climate of the Past, 19, 2257–2286, https://doi.org/10.5194/cp-19-2257-2023, 2023.

Buizert, C., Baggenstos, D., Bereiter, B., Bertler, N., Brook, E. J., and Etheridge, D.: Multi-site ice core Krypton stable isotope ratios, https://doi.org/10.15784/601394, 2020.

Calonne, N., Burr, A., Philip, A., Flin, F., and Geindreau, C.: Effective coefficient of diffusion and permeability of firn at Dome C and Lock In, Antarctica, and of various snow types – estimates over the 100–850 $\mathrm{kg\,m^{-3}}$ density range, The Cryosphere, 16, 967–980, https://doi.org/10.5194/tc-16-967-2022, 2022.

Crotti, I., Landais, A., Stenni, B., Bazin, L., Parrenin, F., Frezzotti, M., Ritterbusch, F., Lu, Z.-T., Jiang, W., Yang, G.-M., et al.: An extension of the TALDICE ice core age scale reaching back to MIS 10.1, Quaternary Science Reviews, 266, 107 078, https://doi.org/10.1016/j.quascirev.2021.107078, 2021.

Epifanio, J. A., Brook, E. J., Buizert, C., Pettit, E. C., Edwards, J. S., Fegyveresi, J. M., Sowers, T. A., Severinghaus, J. P., and Kahle, E. C.: Millennial and orbital-scale variability in a 54 000-year record of total air content from the South Pole ice core, The Cryosphere, 17, 4837–4851, https://doi.org/10.5194/tc-17-4837-2023, 2023.

Etheridge, D. M., Steele, L., Langenfelds, R. L., Francey, R. J., Barnola, J.-M., and Morgan, V.: Natural and anthropogenic changes in atmospheric CO2 over the last 1000 years from air in Antarctic ice and firn, Journal of Geophysical Research: Atmospheres, 101, 4115–4128, https://doi.org/10.1029/95JD03410, 1996.

Extier, T., Landais, A., Bréant, C., Prié, F., Bazin, L., Dreyfus, G., Roche, D. M., and Leuenberger, M.: On the use of δ18Oatm for ice core dating, Quaternary Science Reviews, 185, 244–257, https://doi.org/https://doi.org/10.1016/j.quascirev.2018.02.008, 2018.

Freitag, J., Wilhelms, F., and Kipfstuhl, S.: Microstructure-dependent densification of polar firn derived from X-ray microtomography, Journal of Glaciology, 50, 243–250, https://doi.org/10.3189/172756504781830123, 2004.

Fujita, S., Okuyama, J., Hori, A., and Hondoh, T.: Metamorphism of stratified firn at Dome Fuji, Antarctica: A mechanism for local insolation modulation of gas transport conditions during bubble close off, Journal of Geophysical Research: Earth Surface, 114, https://doi.org/https://doi.org/10.1029/2008JF001143, 2009.

Gregory, S. A., Albert, M. R., and Baker, I.: Impact of physical properties and accumulation rate on pore close-off in layered firn, The Cryosphere, 8, 91–105, https://doi.org/10.5194/tc-8-91-2014, 2014.

Hörhold, M., Kipfstuhl, S., Wilhelms, F., Freitag, J., and Frenzel, A.: The densification of layered polar firn, Journal of Geophysical Research: Earth Surface, 116, https://doi.org/10.1029/2009JF001630, 2011.

Huber, C., Beyerle, U., Leuenberger, M., Schwander, J., Kipfer, R., Spahni, R., Severinghaus, J., and Weiler, K.: Evidence for molecular size dependent gas fractionation in firn air derived from noble gases, oxygen, and nitrogen measurements, Earth and Planetary Science Letters, 243, 61–73, https://doi.org/https://doi.org/10.1016/j.epsl.2005.12.036, 2006.

Ikeda-Fukazawa, T., Kawamura, K., and Hondoh, T.: Mechanism of Molecular Diffusion in Ice Crystals, Molecular Simulation, 30, 973–979, https://doi.org/10.1080/08927020410001709307, 2004.

Kahle, E., Buizert, C., Conway, H., Epifanio, J., Fudge, T. J., and Jones, T. R.: Temperature, accumulation rate, and layer thinning from the South Pole ice core (SPC14), https://doi.org/10.15784/601396, 2020.

Kawamura, K., Parrenin, F., Lisiecki, L., Uemura, R., Vimeux, F., Severinghaus, J. P., Hutterli, M. A., Nakazawa, T., Aoki, S., Jouzel, J., et al.: Northern Hemisphere forcing of climatic cycles in Antarctica over the past 360,000 years, Nature, 448, 912–916, https://doi.org/10.1038/nature06015, 2007.

Landais, A., Barnola, J., Kawamura, K., Caillon, N., Delmotte, M., Van Ommen, T., Dreyfus, G., Jouzel, J., Masson-Delmotte, V., Minster, B., Freitag, J., Leuenberger, M., Schwander, J., Huber, C., Etheridge, D., and Morgan, V.: Firn-air δ15N in modern polar sites and glacial–interglacial ice: a model-data mismatch during glacial periods in Antarctica?, Quaternary Science Reviews, 25, 49–62, https://doi.org/https://doi.org/10.1016/j.quascirev.2005.06.007, 2006.

Landais, A., Dreyfus, G., Capron, E., Pol, K., Loutre, M. F., Raynaud, D., Lipenkov, V. Y., Arnaud, L., Masson-Delmotte, V., Paillard, D., Jouzel, J., and Leuenberger, M.: Towards orbital dating of the EPICA Dome C ice core using delta;O_2/N_2, Climate of the Past, 8, 191–203, https://doi.org/10.5194/cp-8-191-2012, 2012.

Lee, J. E., Brook, E. J., Bertler, N. A. N., Buizert, C., Baisden, T., Blunier, T., Ciobanu, V. G., Conway, H., Dahl-Jensen, D., Fudge, T. J., Hindmarsh, R., Keller, E. D., Parrenin, F., Severinghaus, J. P., Vallelonga, P., Waddington, E. D., and Winstrup, M.: An 83 000-year-old ice core from Roosevelt Island, Ross Sea, Antarctica, Climate of the Past, 16, 1691–1713, https://doi.org/10.5194/cp-16-1691-2020, 2020.

Mulvaney, R., Alemany, O., and Possenti, P.: The Berkner Island (Antarctica) ice-core drilling project, Annals of Glaciology, 47, 115–124, https://doi.org/10.3189/172756407786857758, 2007.

Neff, P. D.: A review of the brittle ice zone in polar ice cores, Annals of Glaciology, 55, 72–82, https://doi.org/10.3189/2014AoG68A023, 2014.

Oyabu, I., Kawamura, K., Kitamura, K., Hirabayashi, M., Aoki, S., Morimoto, S., and Nakazawa, T.: Dome Fuji ice core gas data (112 - 2001m, 15N, O2/N2, Ar/N2), https://doi.org/10.17592/001.2021043001, 2021a.

Oyabu, I., Kawamura, K., Uchida, T., Fujita, S., Kitamura, K., Hirabayashi, M., Aoki, S., Morimoto, S., Nakazawa, T., Severinghaus, J. P., and Morgan, J. D.: Fractionation of O_2/N_2 and Ar/N_2 in the Antarctic ice sheet during bubble formation and bubble–clathrate hydrate transition from precise gas measurements of the Dome Fuji ice core, The Cryosphere, 15, 5529–5555, https://doi.org/10.5194/tc-15-5529-2021, 2021b.

Oyabu, I., Kawamura, K., Buizert, C., Parrenin, F., Orsi, A., Kitamura, K., Aoki, S., and Nakazawa, T.: The Dome Fuji ice core DF2021 chronology (0–207 kyr BP), Quaternary Science Reviews, 294, 107 754, https://doi.org/10.1016/j.quascirev.2022.107754, 2022.

Severinghaus, J.: Nitrogen and Oxygen Gas Isotopes in the Siple Dome and Byrd Ice Cores, Antarctica [Dataset], https://doi.org/10.7265/N55X26V0, 2009.

Severinghaus, J.: Low-res d15N and d18O of O2 in the WAIS Divide 06A Deep Core [Dataset], https://doi.org/10.7265/N5S46PWD, 2015.

Severinghaus, J.: South Pole (SPICECORE) 15N, 18O, O2/N2 and Ar/N2 [Dataset], https://doi.org/10.15784/601152, 2019.

Severinghaus, J. P. and Battle, M. O.: Fractionation of gases in polar ice during bubble close-off: New constraints from firn air Ne, Kr and Xe observations, Earth and Planetary Science Letters, 244, 474–500, https://doi.org/https://doi.org/10.1016/j.epsl.2006.01.032, 2006.

Smith, M. E.: The Pleistocene O2 record in two ice cores, 1998.

Suwa, M. and Bender, M. L.: Chronology of the Vostok ice core constrained by O2/N2 ratios of occluded air, and its implication for the Vostok climate records, Quaternary Science Reviews, 27, 1093–1106, https://doi.org/https://doi.org/10.1016/j.quascirev.2008.02.017, 2008a.

Suwa, M. and Bender, M. L.: O2/N2 ratios of occluded air in the GISP2 ice core, Journal of Geophysical Research: Atmospheres, 113, https://doi.org/https://doi.org/10.1029/2007JD009589, 2008b.

Winski, D. A., Fudge, T. J., Ferris, D. G., Osterberg, E. C., Fegyveresi, J. M., Cole-Dai, J., Thundercloud, Z., Cox, T. S., Kreutz, K. J., Ortman, N., et al.: The SP19 chronology for the South Pole Ice Core–Part 1: volcanic matching and annual layer counting, Climate of the Past, 15, 1793–1808, https://doi.org/10.5194/cp-15-1793-2019, 2019.